The Mesoscale Kinetic Energy Spectrum of a Baroclinic Life Cycle

MICHAEL L. WAITE* AND CHRIS SNYDER

National Center for Atmospheric Research,+ Boulder, Colorado

(Manuscript received 6 May 2008, in final form 6 October 2008)

ABSTRACT

The atmospheric mesoscale kinetic energy spectrum is investigated through numerical simulations of an idealized baroclinic wave life cycle, from linear instability to mature nonlinear evolution and with high horizontal and vertical resolution ($\Delta x \approx 10$ km and $\Delta z \approx 60$ m). The spontaneous excitation of inertia–gravity waves yields a shallowing of the mesoscale spectrum with respect to the large scales, in qualitative agreement with observations. However, this shallowing is restricted to the lower stratosphere and does not occur in the upper troposphere. At both levels, the mesoscale divergent kinetic energy spectrum—a proxy for the inertia–gravity wave energy spectrum—resembles a $-5/3$ power law in the mature stage. Divergent kinetic energy dominates the lower stratospheric mesoscale spectrum, accounting for its shallowing. Rotational kinetic energy, by contrast, dominates the upper tropospheric spectrum and no shallowing of the full spectrum is observed. By analyzing the tendency equation for the kinetic energy spectrum, it is shown that the lower stratospheric spectrum is not governed solely by a downscale energy cascade; rather, it is influenced by the vertical pressure flux divergence associated with vertically propagating inertia–gravity waves.

1. Introduction

More than two decades after the first comprehensive observations of the atmospheric kinetic energy spectrum (Nastrom and Gage 1985), the dynamics of the mesoscale portion remain actively debated. At synoptic scales, where the flow is predominantly quasigeostrophic (QG), the horizontal wavenumber energy spectrum follows a k^{-3} power law (henceforth a -3 spectrum), agreeing with theoretical predictions for QG turbulence (Charney 1971; Boer and Shepherd 1983). At scales below around 500 km—the mesoscale—the QG approximation is less appropriate, and the spectrum shallows to a slope of approximately $-5/3$. In this paper, we investigate the mesoscale spectrum of a high-resolution baroclinic life cycle simulation. Idealized baroclinic waves are known to exhibit many remarkably realistic mesoscale features such as fronts, jets, and inertia–gravity waves (IGWs; e.g., Polavarapu and Peltier 1990; Snyder et al. 1991; Thorncroft et al. 1993; O'Sullivan and Dunkerton 1995; Zhang 2004; Plougonven and Snyder 2005, 2007). Such simulations therefore provide a convenient framework for the study of fundamental mesoscale dynamics in the absence of the complicating effects of moist convection and topography. Here we address the natural question of whether such dynamics are sufficient to yield a kinetic energy spectrum in qualitative agreement with observations.

The mesoscale spectral slope has intrigued researchers because of its agreement with two classical inertial ranges in homogeneous turbulence: the direct energy cascade of three-dimensional turbulence (Kolmogorov 1941) and the inverse energy cascade of two-dimensional turbulence (Kraichnan 1967). Neither of these regimes, however, is appropriate for the mesoscale; nevertheless, compelling analogies have been made between mesoscale dynamics and classical turbulence theories. The atmosphere is on average stably stratified and thus has two distinct modes of motion: quasi-horizontal vortical motion, which has potential vorticity (PV), and IGWs (for a review, see Riley and Lelong 2000). This vortex–wave decomposition underlies many theories of the mesoscale spectrum. Vortical motion, which reduces to vertically decoupled layers of horizontal flow in the

* Current affiliation: Department of Mathematics and Statistics, University of Victoria, Victoria, British Columbia, Canada.

+ The National Center for Atmospheric Research is sponsored by the National Science Foundation.

Corresponding author address: Dr. Michael L. Waite, Department of Mathematics and Statistics, University of Victoria, P.O. Box 3060, Stn CSC, Victoria BC V8W 3R4, Canada.
E-mail: mwaite@mathuvic.ca

DOI: 10.1175/2008JAS2829.1

strongly stratified limit, was hypothesized to cascade energy upscale by analogy with two-dimensional turbulence[1] (Gage 1979; Lilly 1983). IGWs, unconstrained by PV conservation, were conjectured to have a direct energy cascade as in three-dimensional turbulence (Dewan 1979; VanZandt 1982; Dewan 1997). Other theories for a direct cascade have been advanced for QG turbulence (Tung and Orlando 2003), surface QG turbulence (Tulloch and Smith 2006), and anisotropic three-dimensional stratified turbulence (Lindborg 2006). Each of these theories, despite having very different mechanisms, assumes an inertial range cascade (e.g., Lesieur 1997) and predicts a horizontal wavenumber kinetic energy spectrum proportional to $k^{-5/3}$. (The surface QG $-5/3$ spectrum, however, occurs only near the surface and rigid tropopause.)

Observations play an important role in evaluating proposed explanations of the mesoscale spectrum. The scaling of third-order velocity structure functions at length scales below 100 km is consistent with theoretical predictions for downscale energy transfer, casting doubt on the inverse cascade idea (Lindborg and Cho 2001). Horizontally rotational kinetic energy has been found to dominate the mesoscale spectrum in different datasets, implying that the mesoscale spectrum cannot be universally attributed solely to IGWs (Cho et al. 1999; Lindborg 2007). Nevertheless, these observations show significant levels of divergent kinetic energy, and mesoscale IGWs are frequently observed (e.g., Uccellini and Koch 1987; Fritts and Nastrom 1992; Ramamurthy et al. 1993).

Our understanding of the mesoscale spectrum has been advanced by the study of homogeneous turbulence in rotating stratified fluids. Bartello (1995) showed that at small Rossby and Froude numbers, vortical energy develops a relatively steep spectrum associated with a direct cascade of potential enstrophy, whereas wave energy has a shallower spectrum resulting from a direct cascade of energy. Because vortical energy dominates at large scales, these spectra ultimately cross and a transition from a steep to shallow spectrum results. The vortical motion appears to catalyze the downscale transfer of wave energy, with the transfer spectrum dominated by the wave–wave–vortex triad interactions identified by Lelong and Riley (1991).

A number of studies have investigated strongly stratified vortical motion with weak or no rotation as a first approximation to dry mesoscale dynamics. Simulations employing small-scale forcing have demonstrated the inability of vortical modes to cascade energy upscale at large Rossby numbers (Herring and Métais 1989; Lilly et al. 1998). This evidence—along with the structure function analysis of Lindborg and Cho (2001) and related statistical mechanical arguments (Waite and Bartello 2004)—overwhelmingly points to the downscale transfer of mesoscale kinetic energy. With sufficiently high resolution, stratified turbulence dominated by large-scale vortical motion has approximately a $-5/3$ spectrum (Riley and de Bruyn Kops 2003; Waite and Bartello 2004; Lindborg 2006; Kitamura and Matsuda 2006). This spectrum requires a vertical dissipation scale smaller than $O(U/N)$, where U is the root-mean-square (RMS) velocity and N is the Brunt–Väisälä frequency (Waite and Bartello 2004; Lindborg 2006; Brethouwer et al. 2007). As foreseen by Lilly (1983), shear instabilities develop on this scale and appear to play a crucial role in the shallowing of the spectrum. In the atmosphere, $U/N \sim O(1)$ km; thus, resolving this scale requires a vertical grid spacing $\Delta z \lesssim O(100)$ m.

Other studies have endeavored to simulate the atmospheric mesoscale and its energy spectrum directly with more comprehensive atmospheric models. These simulations generally include physical processes absent in the stratified turbulence simulations, such as topographic IGW generation, moist convection, and more realistic background temperature profiles. Both high-resolution general circulation models (GCMs; Koshyk and Hamilton 2001; Takahashi et al. 2006; Hamilton et al. 2008) and mesoscale numerical weather prediction (NWP) models (Skamarock 2004; Skamarock and Klemp 2008) have successfully captured the transition from a large-scale -3 spectrum to a shallower mesoscale spectrum. The kinetic energy spectra of Koshyk and Hamilton (2001) and Hamilton et al. (2008) are dominated by horizontally rotational motion in the troposphere, even in the mesoscale. By contrast, Skamarock and Klemp (2008) found approximately equal contributions from rotational and divergent motion. Intriguingly, Takahashi et al. (2006) and Hamilton et al. (2008) demonstrated the emergence of a relatively shallow mesoscale spectrum for dry dynamical core experiments without moist convection or topography, although the amount of mesoscale energy in these simulations was greatly reduced. The ability of atmospheric models to produce realistic spectra is not universal, however; some models consistently have mesoscale spectra much steeper than $-5/3$, apparently because of the formulation of the numerical scheme (e.g., Shutts 2005).

[1] Vortical motion is sometimes described as quasi-two-dimensional; however, although it is predominantly horizontal, it can develop strong vertical shear, making it decidedly three-dimensional. At large scales, it is equivalent to the balanced component of the flow.

The present study is motivated by the ambiguous connection between the stratified turbulence and atmospheric simulations. Horizontally divergent motion appears to make up a significant part of the mesoscale spectrum, underscoring the possibility that a downscale cascade of inertia–gravity wave energy is at least partially responsible for the observed spectra. However, it is unclear whether these waves are directly forced in the mesoscale (for example, by convection or topography) or whether they are generated by nonlinear interactions with the vortical flow, as in stratified turbulence simulations with vortical forcing or initial conditions. A baroclinic life cycle—the archetype of midlatitude vortical motion—is known to spontaneously generate IGWs, both at the surface front (Snyder et al. 1993) and near the upper-level jet (O'Sullivan and Dunkerton 1995; Zhang 2004; Plougonven and Snyder 2005, 2007). Plougonven and Snyder (2005) showed that the upper-level waves appear to be trapped in the vortical flow, in agreement with the wave-capture model of Bühler and McIntyre (2005). The strain field of the vortex contracts the wavelengths of the trapped IGWs, transferring their energy downscale in a physical process reminiscent of the spectral wave–wave–vortex interaction of Lelong and Riley (1991) and Bartello (1995).

Does a nonlinear baroclinic wave develop a mesoscale $-5/3$ energy spectrum without the direct forcing of the mesoscale by convection and topography? Recent GCM studies (Takahashi et al. 2006; Hamilton et al. 2008) have shown that dry mesoscale dynamics can produce a $-5/3$ spectrum, but with a much-reduced amplitude. Here, we take a closer look at this question by examining the mesoscale spectrum and spectral energy budget of an idealized baroclinic life cycle. The setup (section 2) is a natural extension of rotating stratified turbulence simulations to a more realistic atmosphere with a troposphere and lower stratosphere. In section 3a we present kinetic energy spectra of the simulations, in section 3b we investigate the contributions to the spectra from horizontally rotational and divergent velocity, in section 3c we compare zonal wavenumber kinetic and potential energy spectra with observations, and in section 3d we use kinetic energy transfer spectra to examine the extent to which the mesoscale is an inertial range. Even in the idealized setting considered here, direct forcing of the mesoscale by vertically propagating IGWs is shown to occur at some levels. Discussion and conclusions are given in section 4.

2. Dynamical equations and numerical setup

We employ the Advanced Research core of the Weather Research and Forecast (WRF) model (Skamarock et al. 2005), which integrates the equations for a nonhydrostatic compressible atmosphere in flux form with terrain-following hydrostatic pressure η as the vertical coordinate.[2] The equations of motion, expressed in height coordinates and neglecting moisture effects, are

$$\frac{D\mathbf{u}}{Dt} + f\,\hat{\mathbf{e}}_3 \times \mathbf{u} = -\frac{1}{\rho}\nabla p' + \mathcal{D}_{\mathbf{u}}, \tag{1}$$

$$\frac{Dw}{Dt} = -\frac{1}{\rho}\partial_z p' - g\frac{\rho'}{\rho} + \mathcal{D}_w, \tag{2}$$

$$\frac{D\theta}{Dt} = \mathcal{D}_\theta, \quad \text{and} \tag{3}$$

$$\frac{D\rho}{Dt} + \rho\,(\nabla \cdot \mathbf{u} + \partial_z w) = 0, \tag{4}$$

where $\mathbf{u}$ is the horizontal velocity, w is the vertical velocity, $\nabla = (\partial_x, \partial_y)$ is the horizontal gradient, $D/Dt = \partial_t + \mathbf{u} \cdot \nabla + w\,\partial_z$ is the material derivative, $\hat{\mathbf{e}}_3$ is the vertical unit vector, ρ is the density, p is the pressure, θ is the potential temperature, g is the gravitational acceleration, f is the Coriolis parameter, and $\mathcal{D}_q$ denotes the dissipation of q. Primes denote fluctuations from the hydrostatic reference states $\bar{p}(z)$ and $\bar{\rho}(z)$.

Our domain is an f plane of dimensions $L_x = 4000$ km, $L_y = 10\,000$ km, and $L_z = 20$ km, with $f = 10^{-4}$ s^{-1}. Boundary conditions are periodic in x and rigid and symmetric in y and z; that is, the normal derivatives of scalars and boundary-parallel velocity are zero. As a result, there are no sources or sinks of energy at the boundaries. The surface is flat at $z = 0$, and no boundary layer parameterization is employed. The horizontal grid spacing and time step are $\Delta x = \Delta y = 12.5$ km and $\Delta t = 50$ s. Motivated by recent findings in rotating stratified turbulence (Lindborg 2006; Waite and Bartello 2006b) and by the need to resolve sloping frontal structures (e.g., Snyder et al. 1993), we employ a fine vertical grid with $\Delta z \approx 62.5$ m. Lower-resolution simulations with $\Delta x = 25$ and 50 km were also performed, for which Δz and Δt were increased accordingly.

The dissipation terms $\mathcal{D}_q$ are given by a sixth-order horizontal filter $K_{\text{bot}}(\partial_x^6 + \partial_y^6)$ in the lowest 2.5 km to control the scale collapse associated with frontogenesis and by a second-order eddy viscosity sponge layer $K_{\text{top}}(\partial_x^2 + \partial_y^2)$ in the upper 4 km to minimize the reflection of IGWs off the upper boundary (note that the

[2] We use exponentially stretched η levels in our simulations, yielding nearly constant vertical spacing in height. For clarity, we formulate our presentation and analysis in terms of the vertical height coordinate, linearly interpolating model output from η to z levels as necessary.

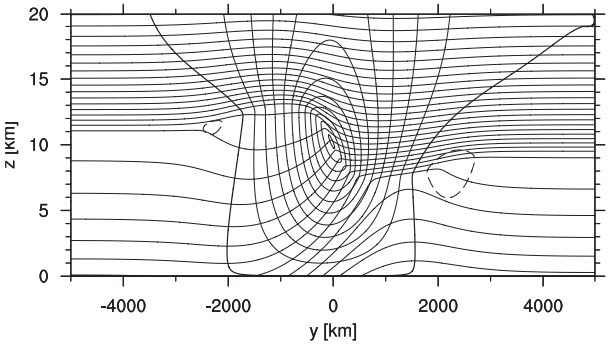

FIG. 1. Vertical (y–z) slice of the initial jet, showing θ and u. Contour intervals are 5 K for θ and 5 m s^{-1} for u. The zero velocity contour is bold; negative contours are dashed.

derivatives in $\mathcal{D}_q$ are computed holding η, not z, fixed). In both cases, the diffusion coefficient is maximum at the boundary and goes to zero as a cosine. The dissipation time scales at the lower and upper boundaries are $\Delta x^6/K_{\text{bot}} = 1.8$ h and $\Delta x^2/K_{\text{top}} = 1.4$ h, respectively. No explicit diffusion is employed in the interior, where the implicit sixth-order filter associated with the discretization of the horizontal momentum flux provided sufficient dissipation to prevent the accumulation of energy at the grid scale (see Wicker and Skamarock 2002). Explicit vertical diffusion is not included.

We initialize our simulations with a baroclinically unstable zonal jet following Plougonven and Snyder (2005). A constant PV troposphere of 0.4 potential vorticity units (PVU; 1 PVU $\equiv 10^{-6}$ m^2 s^{-1} K kg^{-1}) and stratosphere of 4 PVU are separated by a prescribed tropopause. The PV is then inverted for the geostrophically balanced zonal velocity and temperature (see Fig. 1). This procedure yields a maximum velocity of 56 m s^{-1} (Fig. 1) and a maximum Brunt–Väisälä frequency $N = 0.02$ s^{-1} (Fig. 6). The RMS Rossby number Ro $\equiv |\zeta|/f$ and Froude number Fr $\equiv S/N$ averaged over $L_z/4 \le z \le 3L_z/4$ and $-L_y/4 \le y \le L_y/4$ are both ≈ 0.2, where ζ is the vertical component of vorticity and S is the vertical shear. The jet is perturbed with the fastest-growing gravest normal mode with small amplitude (0.1 K for θ). The normal mode is computed iteratively by applying a small perturbation to the jet, running the model for 4 days, scaling down the perturbation, and repeating until exponential growth is achieved; three iterations are performed. The simulation is then integrated for 13 days, with fields output every 3 h.

3. Results

The evolution of the baroclinic wave follows the canonical cyclonic life cycle extensively documented in the literature (e.g., Polavarapu and Peltier 1990; Snyder et al. 1991; Thorncroft et al. 1993). The perturbation grows exponentially for the first 8 days, with a growth rate of approximately (32 h)$^{-1}$. The fully developed flow is relatively strong, with RMS wind speeds and Rossby numbers of around 20 m s^{-1} and 0.5, respectively. The corresponding maximum values of $|\mathbf{u}|$ and Ro are 70 m s^{-1} and 5 (see Table 1).

TABLE 1. Daily averaged RMS and maximum wind speed (m s^{-1}) and Rossby number. Values are computed over $-L_y/4 \le y \le L_y/4$ and $L_z/4 \le z \le 3L_z/4$.

Day	RMS $\lvert\mathbf{u}\rvert$	Maximum $\lvert\mathbf{u}\rvert$	RMS Ro	Maximum Ro
8	22	64	0.37	4.4
9	23	68	0.47	5.1
10	24	72	0.53	5.6
11	25	76	0.56	5.7
12	25	75	0.55	5.9

The vertical component of vorticity $\zeta \equiv \partial_x v - \partial_y u$ and horizontal divergence $\delta \equiv \partial_x u + \partial_y v$ (henceforth simply vorticity and divergence, respectively) for $t = 9$–12 days are plotted at $z = 9$ km (Fig. 2) and 13 km (Fig. 3). Over $t = 9.5$–10.5 days, three classes of IGWs appear, most prominently in the divergence field at $z = 13$ km. First, a long band is located east of the trough, which is excited by frontogenesis near the surface (Snyder et al. 1993). Second, a small wave packet is visible west of the ridge, which resembles that described by Zhang (2004) and appears to have a source in the upper tropospheric jet. Third, a long, narrow wave packet extends from ridge to trough; Plougonven and Snyder (2005, 2007) showed that the structure of these waves is consistent with their propagation through the deformation and shear of the baroclinic vortex. These waves are labeled respectively I, II, and III in Fig. 3d. The identification of these mesoscale divergence patterns—and consequently the mesoscale kinetic energy of the horizontally divergent velocity field—with IGWs is supported by dispersion relation analyses in analogous and closely related numerical simulations (e.g., Zhang 2004; Plougonven and Snyder 2007; Snyder et al. 2007; Viudez 2007). There is also a significant wave signature in the vorticity field, especially at $z = 13$ km where the vorticity of the baroclinic wave is weaker. This signal is consistent with the near-inertial frequencies of the type-II and -III waves [see Plougonven and Snyder (2007) for more discussion]. The spatial extent of the wave packets increases markedly as the baroclinic wave evolves. By $t = 12.5$ days, the waves cover the entire vortex as well as the adjacent straining region.

The vertical structure of the flow through the $y = 0$ plane is illustrated in Fig. 4 for $t = 9$–12 days. The potential temperature field (left panel, with the 1 PVU

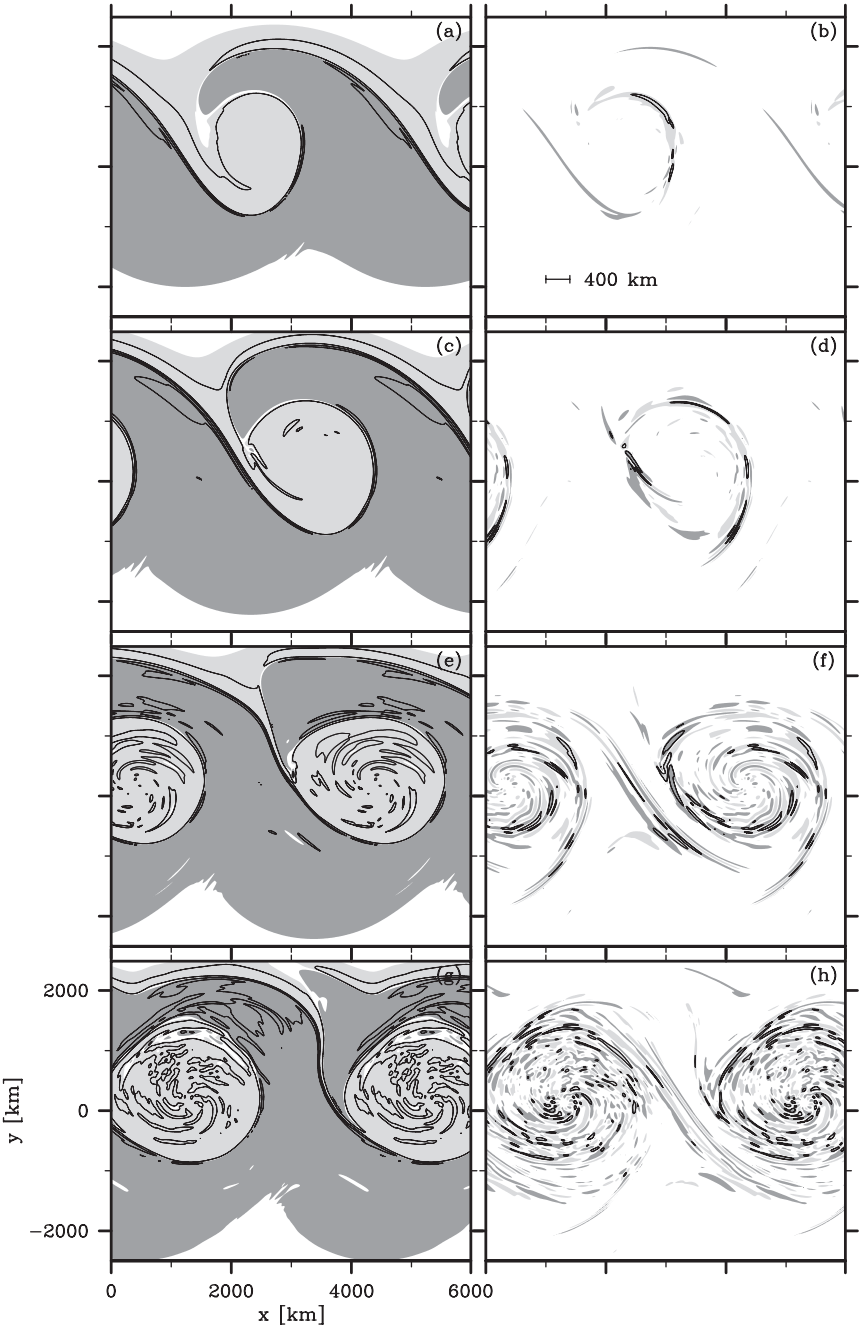

FIG. 2. (left) Vorticity ζ and (right) divergence δ at day (a),(b) 9.5, (c),(d) 10.5, (e),(f) 11.5, and (g),(h) 12.5, at $z = 9$ km. Contours are drawn at $\pm 0.6f$. Values less than $-0.2f$ are dark gray; values greater than $0.2f$ are light gray. For clarity, an extra half wavelength is included in x and the y range is restricted to $-2500 \leq y \leq 2500$ km.

contour of PV superposed) exhibits the familiar displacement of the tropopause on the synoptic scale of the baroclinic wave and the smaller scales of fronts, tropopause folds, and PV filaments (e.g., Bush and Peltier 1994; Rotunno et al. 1994). Mesoscale fluctuations in θ in the troposphere, many of which are collocated with filaments of high-PV air, increase in amplitude as the wave evolves. In the lower stratosphere, θ perturbations from vertically propagating IGWs are clearly visible. The right panel of Fig. 4 shows the normal component of horizontal vorticity: $\omega_y = \partial_z u - \partial_x w$. For $t = 9.5$–10.5 days, bands of vorticity appear in the lower stratosphere,

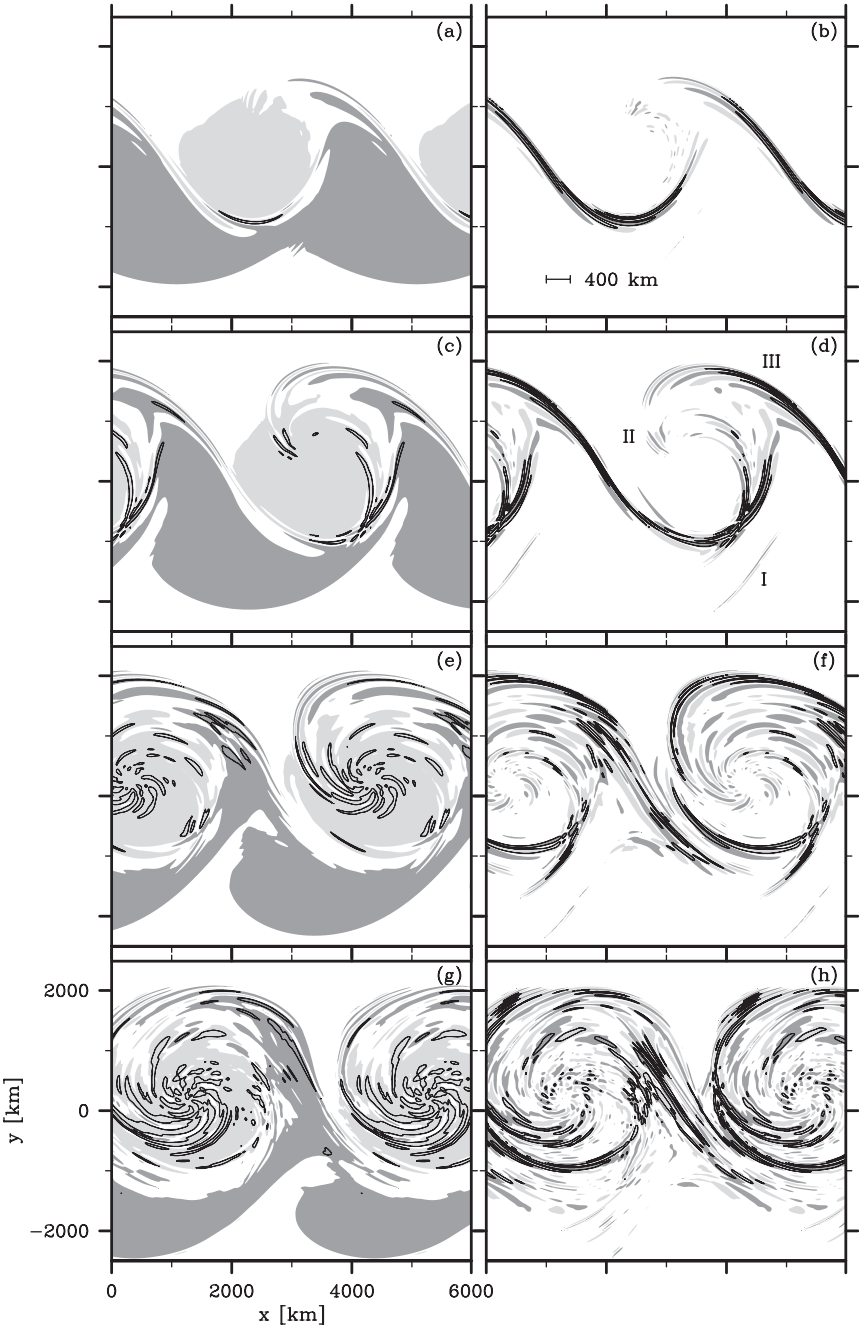

FIG. 3. As in Fig. 2, but at $z = 13$ km.

corresponding to the type-III IGWs discussed above (Plougonven and Snyder 2005, 2007). By around $t = 11.5$ days this coherent packet structure gives way to a more random arrangement of ω_y. A layered vorticity structure emerges in the stable regions of the lower stratosphere with a vertical scale of $O(1)$ km. The tilting of these layers with respect to the isentropes suggests that they result from vertically propagating waves rather than layerwise stratified vortical motion. The upper troposphere, by contrast, is remarkably quiescent.

a. Kinetic energy spectra

Horizontal kinetic energy spectra are computed by performing two-dimensional discrete Fourier transforms (denoted by $\mathcal{F}$) of velocity at each vertical level. A field q yields spectral coefficients $\hat{q}(\mathbf{k})$, where $\mathbf{k} \equiv (k_x, k_y)$ is the

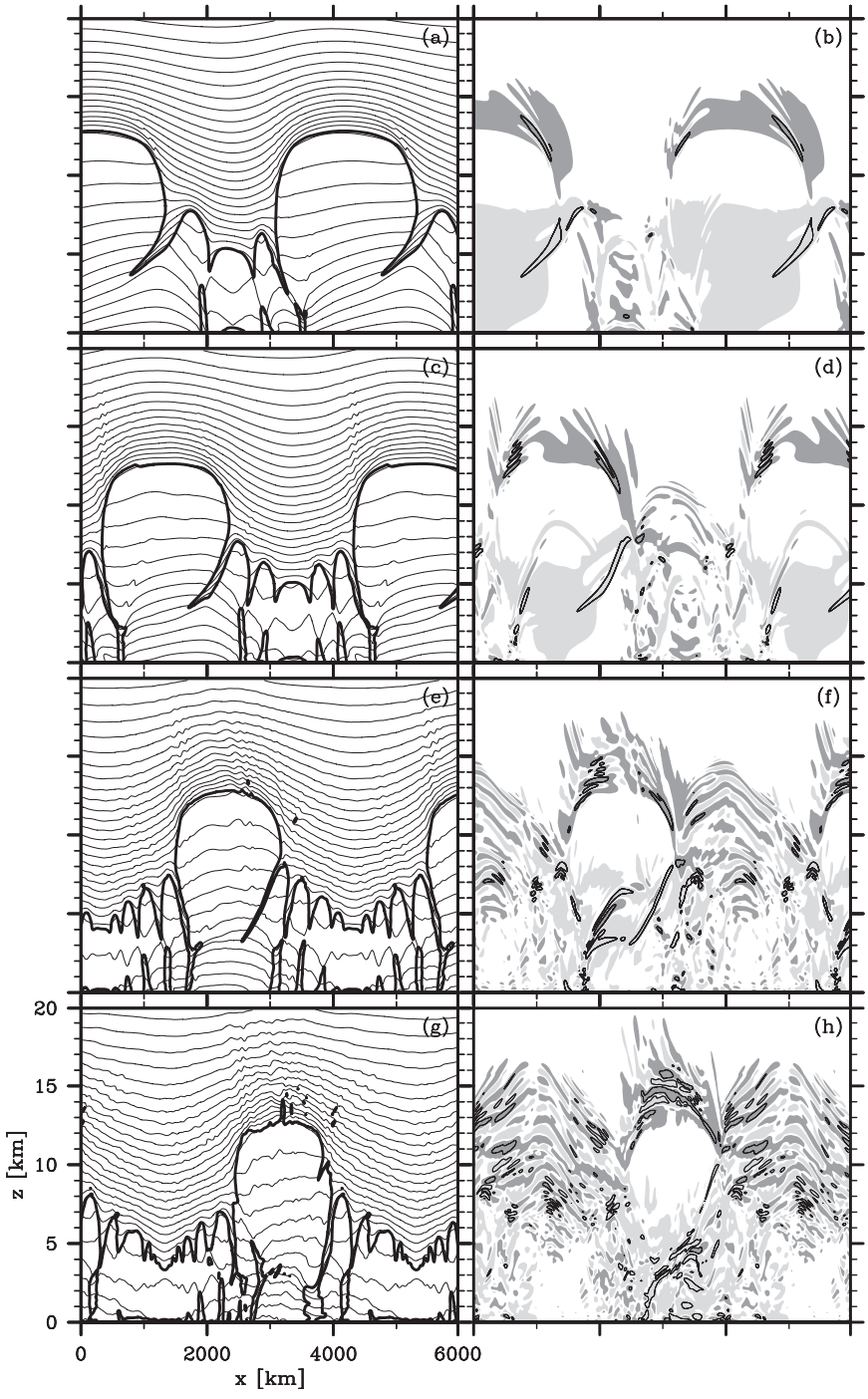

FIG. 4. Vertical (x–z) slices of (left) θ and (right) ω_y at $y = 0$ and day (a),(b) 9.5, (c),(d) 10.5, (e),(f) 11.5, and (g),(h) 12.5. For θ, the contour interval is 5 K; the 1 PVU contour of PV is also shown (thick solid line). For ω_y, contours are drawn at ± 0.01 s^{-1}, with values less than -0.002 s^{-1} dark gray and greater than 0.002 s^{-1} light gray.

horizontal wave vector, and dependence of spectral quantities on z and t is suppressed for clarity. The meridional transform is computed by exploiting the symmetry at the boundary to obtain y-periodic fields with period $2L_y$.

To facilitate the comparison of the kinetic energy spectra at different levels, we consider energy per unit volume. The domain-averaged kinetic energy per unit volume is

$$E_K \equiv \frac{1}{V}\iiint \frac{1}{2}[\rho(\mathbf{u}\cdot\mathbf{u} + w^2)]dV, \tag{5}$$

where V denotes the volume of the domain. As a cubic quantity in the unknowns, the spectrum of E_K is a complicated sum over triads of wave vectors. However, if we replace ρ with $\bar{\rho}$ and furthermore neglect the vertical kinetic energy, which is several orders of magnitude smaller than the horizontal, we can approximate the modal kinetic energy spectrum as

$$E(\mathbf{k}) = \frac{1}{2}\bar{\rho}\hat{\mathbf{u}}\cdot\hat{\mathbf{u}}^*, \tag{6}$$

where * denotes complex conjugate (as does c.c. below). The horizontal wavenumber spectrum $E(k_h)$, where $k_h^2 = k_x^2 + k_y^2$, is obtained in the standard way by angular averaging over wavenumber bands $k_n - \Delta k/2 \le k_h < k_n + \Delta k/2$, where $k_n = 2\pi n/L_x$, $\Delta k = 2\pi/L_x$, and $n = 1, 2, 3, \ldots$ (e.g., Waite and Bartello 2004). Below we make use of the dimensionless wavenumber $k \equiv k_h(L_x/2\pi)$. Observations typically yield one-dimensional spectra such as the zonal wavenumber spectrum $E(k_x)$; for statistically axisymmetric flows with power-law spectra, $E(k_h)$ and $E(k_x)$ are proportional at all but the smallest wavenumbers.

The total kinetic energy spectra, averaged over z = 0–2, 4–6, 8–10, and 12–14 km (henceforth lower troposphere, midtroposphere, upper troposphere, and lower stratosphere, respectively) are plotted in Fig. 5 for t = 8–13 days. The spectra fall off rapidly for $k \lesssim 50$ because of the sixth-order implicit dissipation of the model; this dissipation range moves to larger k_h as the resolution increases and ensures that the flow is not contaminated by underresolved features. We focus our attention on the range of well-resolved wavenumbers $k \lesssim 50$.

In the lower troposphere (Fig. 5a), where strong surface fronts are present, the energy spectrum does not have a constant slope; rather, it approaches a shape that is shallower than -3 over the large-scale end of the mesoscale ($3 \lesssim k \lesssim 10$) and approximately -3 at smaller scales ($10 \lesssim k \lesssim 50$). The midtropospheric spectrum (Fig. 5b) develops a distinct peak around $k = 10$ and an approximately -3 slope at larger wavenumbers. The lower and midtroposphere spectral slopes are approximately equal for $k > 10$, in contrast to the dry dynamical core simulations of Hamilton et al. (2008), who found the mesoscale spectrum to be shallower in the lower troposphere than in the midtroposphere. These spectra are likely influenced by the presence of secondary instabilities in the potential vorticity spiral of the baroclinic wave (as in Methven and Hoskins 1998); these instabilities decay above $z \approx 5$ km and are therefore not apparent in Figs. 2 and 3.

In the upper troposphere (Fig. 5c), the spectrum approaches a slope slightly steeper than -3 from synoptic scales through the mesoscale, with no mesoscale shallowing apparent at any time. Similar findings at synoptic scales were reported by Methven and Hoskins (1998). In the lower stratosphere, on the other hand, the spectrum possesses a clear transition to a shallower slope in the mesoscale. Over t = 8–9 days, the energy spectrum grows significantly for $k > 10$, corresponding to wavelengths less than 400 km. This increase in energy at small scales is consistent with the predominance of fine scales, between 400 km and the dissipation scale, in the divergence and vorticity fields at these times (Figs. 3a,b). Note that the amplitude of the divergence at this level (Fig. 3b) is much larger than that in the upper troposphere (Fig. 2b), consistent with the lack of shallowing in the upper tropospheric spectrum. For t = 9.5–10.5 days, the mesoscale spectrum grows more slowly than at earlier times and is less steep than $-5/3$. Nevertheless, over these times the amplitudes of the divergence and vorticity disturbances continue to grow (Figs. 3c,d). For t = 10.5–12 days, the spectrum grows and steepens, filling in the mesoscale range of wavenumbers from k = 5–50 and approaching a spectrum resembling $-5/3$. This evolution in the lower stratospheric spectrum occurs as the IGW structure changes from localized coherent packets to broad envelopes filling the entire area of the baroclinic vortex (Figs. 3e–h).

In what follows, we take a closer look at the energy spectra of the upper troposphere and lower stratosphere over two time intervals, t = 9.5–10.5 days and 12–13 days, during which the spectrum is approximately stationary (Fig. 5). The vertical profile of N^2, averaged in x along $y = 0$, is plotted in Fig. 6 for both time intervals.

b. Rotational and divergent kinetic energy spectra

The kinetic energy at wave vector $\mathbf{k}$ has an elementary decomposition into horizontally rotational and divergent contributions $E_R(\mathbf{k})$ and $E_D(\mathbf{k})$, which are given by

$$E_R(\mathbf{k}) = \frac{1}{2}\bar{\rho}\frac{|\hat{\zeta}|^2}{k_h^2} \quad \text{and} \tag{7}$$

$$E_D(\mathbf{k}) = \frac{1}{2}\bar{\rho}\frac{|\hat{\delta}|^2}{k_h^2}. \tag{8}$$

The horizontal wavenumber spectra $E_R(k_h)$ and $E_D(k_h)$ are defined analogously to $E(k_h)$. The rotational and divergent kinetic energy spectra, averaged over the upper troposphere and lower stratosphere over the time intervals of interest, are shown in Fig. 7.

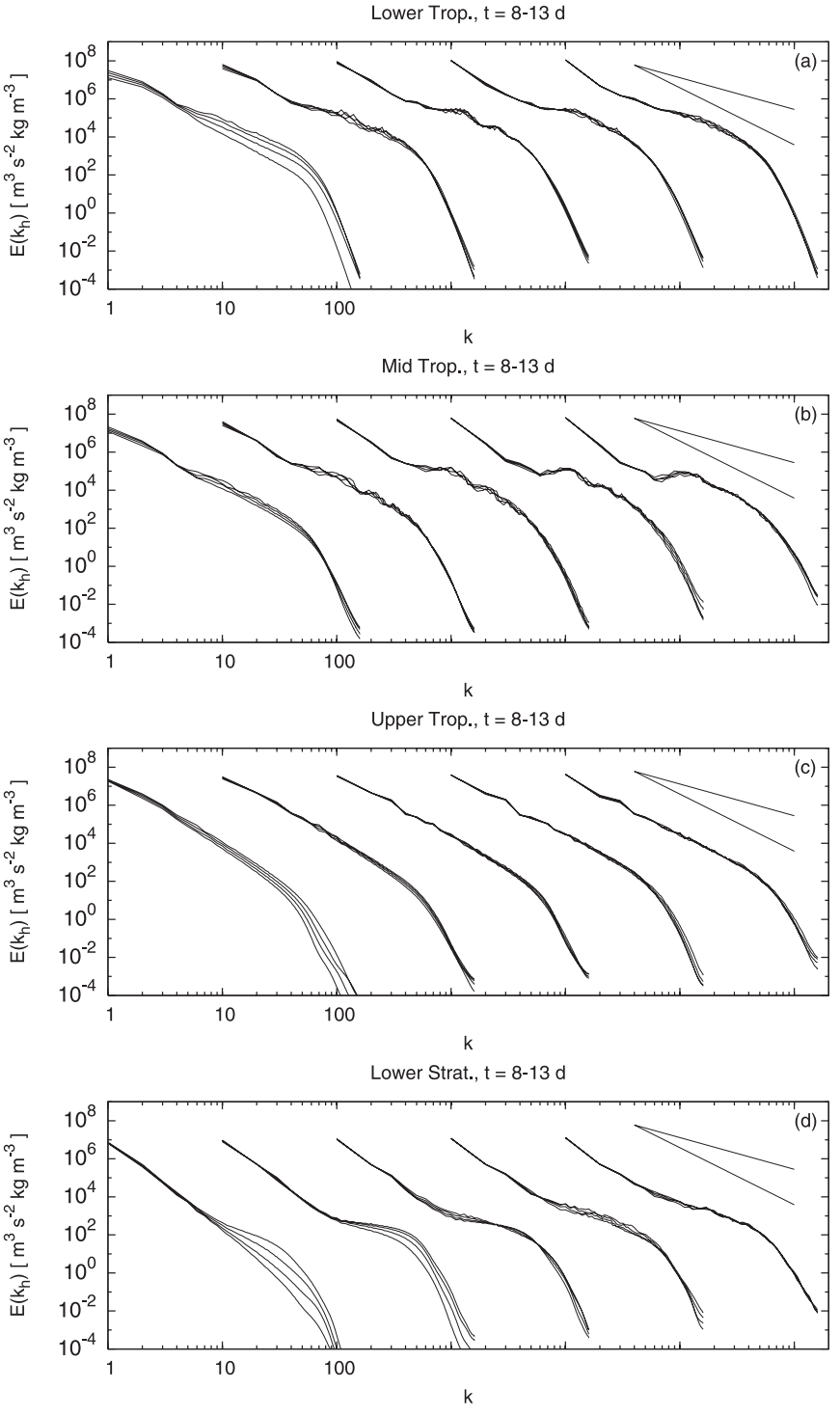

FIG. 5. Horizontal wavenumber spectra of kinetic energy $E(k_h)$ for $t = 8$–13 days, averaged in the vertical over the (a) lower troposphere, (b) midtroposphere, (c) upper troposphere, and (d) lower stratosphere. Spectra are plotted every 6 h and spectra on different days are offset by powers of 10 in k, with later days to the right of earlier days. The reference lines have slopes of $-5/3$ and -3.

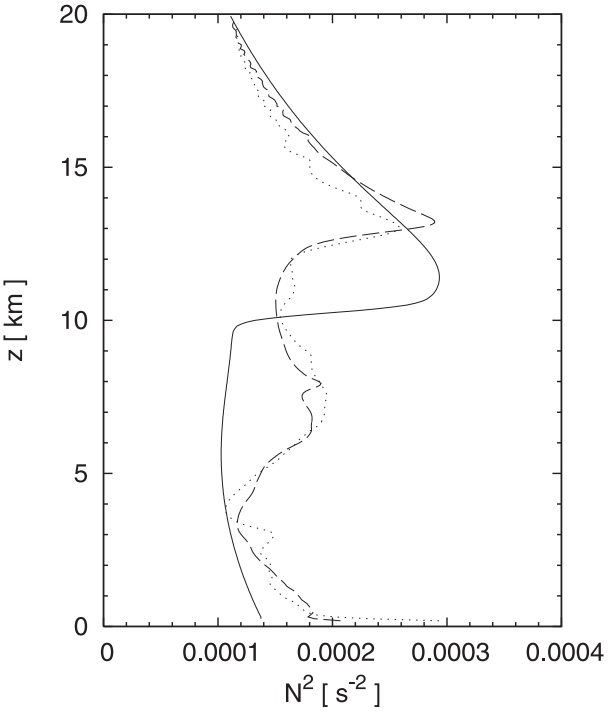

FIG. 6. Vertical profile of zonally averaged N^2 at $y = 0$ for $t = 0$ (solid) and averaged over $t = 9.5$–10.5 days (dashed) and 12–13 days (dotted).

In the upper troposphere, the divergent kinetic energy spectrum has a spectral slope of around -2.6 during the early period, shallowing to -1.7 during the later period.[3] At both times it is markedly shallower than the rotational spectrum, which has a slope of -3.5 and -3.3, respectively, over the two time intervals. The amplitude of the divergent spectrum, however, is too small to influence the slope of the total kinetic energy spectrum, accounting for the lack of spectral transition in Fig. 5c.

The spectra in the lower stratosphere are quite different. Over both time intervals, the divergent kinetic energy spectrum crosses the rotational spectrum at $k \approx 10$, accounting for the transition in the total spectrum seen in Fig. 5d. For $t = 9.5$–10.5 days, the mesoscale portion of the divergent spectrum is extremely shallow, with a slope of around -0.87. The rotational spectrum also shallows in the mesoscale from its large-scale slope of -4.4, although not nearly to the same extent as the divergent spectrum. For $t = 12$–13 days, the rotational spectrum has a slope of -3.7, with weak but apparent shallowing in the mesoscale. The divergent spectrum has a much shallower spectrum of -1.8.

During this later period the divergent mesoscale spectrum is nearly identical in the upper troposphere and lower stratosphere, underscoring the strong connection between the divergent modes at different levels (Fig. 8). The increased resemblance of the divergent kinetic energy spectra in the upper troposphere and lower stratosphere occurs as the IGW field evolves from a few isolated packets to a broad spectrum of waves. It is the decrease in amplitude with height of the rotational spectrum—to the extent that it falls below the shallower divergent spectrum in the mesoscale—that accounts for emergence of the spectral transition in the lower stratosphere.

The $-5/3$ spectrum of divergent kinetic energy is suppressed when lower numerical resolution is employed. In Fig. 9, we plot the lower stratospheric spectra of rotational and divergent energy from simulations with $\Delta x = 12.5$, 25, and 50 km. The $-5/3$ spectral range of divergent kinetic energy and the weak mesoscale shallowing of rotational kinetic energy that are observed for $\Delta x = 12.5$ km are present for $\Delta x = 25$ km but not for $\Delta x = 50$ km. Similar behavior is observed at lower resolution in the upper troposphere. The agreement of the $\Delta x = 25$ km and 12.5 km spectra for $k < 30$ gives us confidence that our mesoscale results are robust.

c. Comparison with observations

The mesoscale in our simulations has significantly less energy than is observed in the atmosphere. In Fig. 10 we compare our upper tropospheric and lower stratospheric kinetic energy spectra against the reference spectrum obtained from Measurement of Ozone and Water Vapor by Airbus In-Service (MOZAIC) data by Lindborg (1999). To facilitate comparison we plot one-dimensional zonal wavenumber spectra of kinetic energy per unit mass, averaged in y over $-L_y/4 \le y \le L_y/4$; these spectra are qualitatively similar to the two-dimensional spectra considered above. In the upper troposphere, the large-scale kinetic energy in our simulations is of the same order of magnitude as the MOZAIC data, although it is systematically smaller at all but the gravest wavenumber. Further restricting the y average to a narrower range band inside the jet leads to good agreement for $k_x \lesssim 10^{-5}$ m^{-1}, confirming that the level of synoptic-scale kinetic energy in the baroclinic wave is consistent with observations. The mesoscale, however, is significantly underenergized. In the upper troposphere, the mesoscale kinetic energy spectrum is steeper than the Lindborg (1999) spectrum and consequently has a much lower amplitude. In the lower stratosphere, the total kinetic energy spectrum follows

[3] Spectral slopes are computed by a least squares power-law fit over one of three wavenumber ranges, depending on whether a spectral transition occurs: $k = 1$–40 for both rotational and divergent spectra in the upper troposphere, where there is no transition; $k = 1$–10 for rotational spectra in the lower stratosphere; and $k = 10$–40 for divergent spectra in the lower stratosphere.

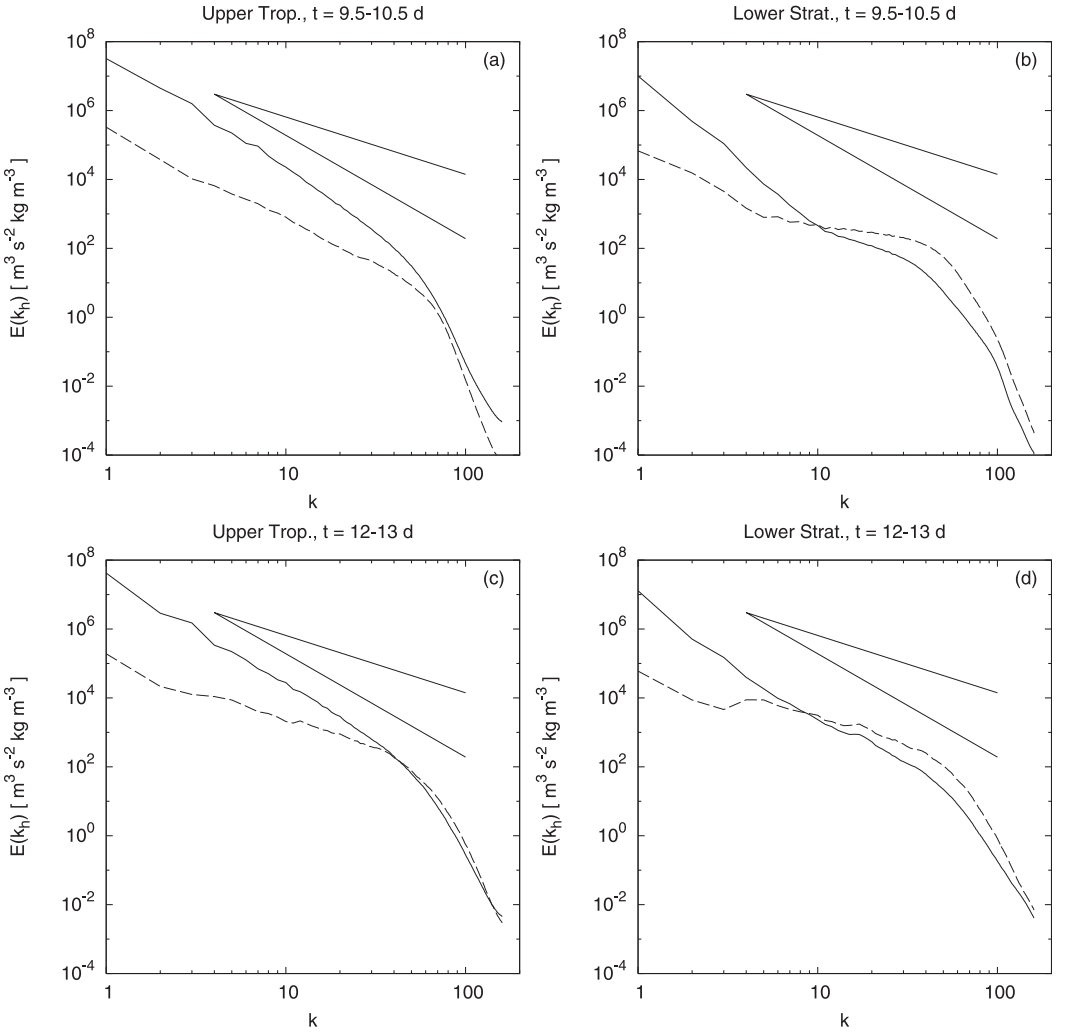

FIG. 7. Horizontal wavenumber spectra of rotational $E_R(k_h)$ (solid) and divergent $E_D(k_h)$ (dashed) kinetic energy, averaged in the vertical over the (left) upper troposphere and (right) lower stratosphere and in time over $t =$ (a),(b) 9.5–10.5 days and (c),(d) 12–13 days.

the reference spectrum, although again with a smaller amplitude.

Figure 10 also shows the zonal wavenumber spectrum of potential energy per unit mass, which is given by

$$E_P(\mathbf{k}) = \frac{1}{2}\frac{g^2}{N_0^2\theta_0^2}\hat{\theta}\cdot\hat{\theta}^*, \tag{9}$$

where N_0 and θ_0 are reference values for the Brunt–Väisälä frequency and potential temperature. These values are computed from temporal and spatial averages of N^2 and θ over the times, levels, and latitudes indicated, yielding $g^2/(N_0^2\theta_0^2) = 5.0$ in the upper troposphere and 2.4 in the lower stratosphere. The shape of the mesoscale potential energy spectrum resembles that of kinetic energy: it is steeper than $-5/3$ in the upper troposphere and consistent with $-5/3$ in the lower stratosphere. At both levels, the ratio of mesoscale kinetic to potential energy is approximately 2. This ratio is in remarkably good agreement with observations (e.g., Gage and Nastrom 1986), despite the overly steep spectrum in the upper troposphere.

d. Spectral kinetic energy budget

We can gain insight into the dynamics of the horizontal wavenumber kinetic energy spectrum by examining the spectrum of its tendency. The evolution of $E(\mathbf{k})$ is given by

$$\frac{\partial}{\partial t}E(\mathbf{k}) = T(\mathbf{k}) + P(\mathbf{k}) + D(\mathbf{k}), \tag{10}$$

where $T(\mathbf{k})$ is the energy transfer due to advection,

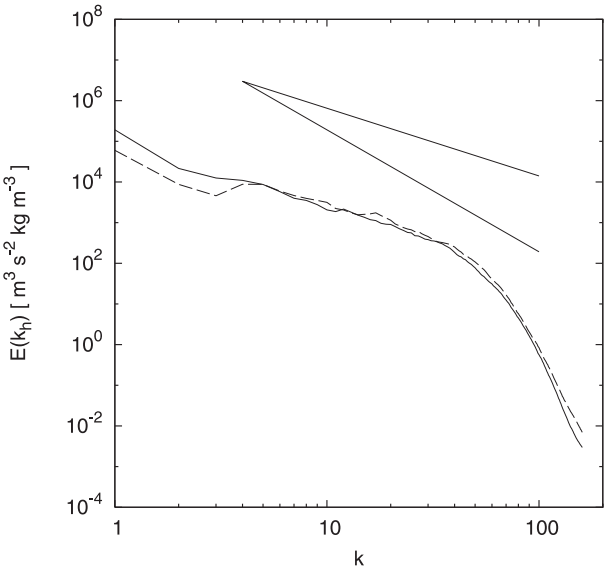

FIG. 8. Horizontal wavenumber spectra of divergent kinetic energy $E_D(k_h)$, averaged in the vertical over the upper troposphere (solid) and lower stratosphere (dashed) and in time over $t = 12$–13 days.

$$T(\mathbf{k}) \equiv -\frac{1}{2}\bar{\rho}\hat{\mathbf{u}}^* \cdot \mathcal{F}(\mathbf{u} \cdot \nabla\mathbf{u} + w\,\partial_z\mathbf{u}) + \text{c.c.}, \tag{11}$$

$P(\mathbf{k})$ is the spectral tendency due to the horizontal pressure gradient (henceforth the pressure term),

$$P(\mathbf{k}) \equiv -\frac{1}{2}\bar{\rho}\hat{\mathbf{u}}^* \cdot \mathcal{F}\left(\frac{1}{2}\nabla p'\right) + \text{c.c.}, \tag{12}$$

and $D(\mathbf{k})$ is the dissipation. Away from the upper and lower boundaries, $D(\mathbf{k})$ is given by the implicit dissipation of the numerical scheme, which approximates the form $\partial_x^6 + \partial_y^6$ and is therefore expected to be negligible at all but the largest wavenumbers.

Unlike its counterpart in two- and three-dimensional turbulence, the level-by-level transfer $T(\mathbf{k})$ is not strictly conservative; that is, its sum over $\mathbf{k}$ is not necessarily zero. In addition to the conservative exchange of kinetic energy between different wavenumbers, $T(\mathbf{k})$ has a contribution from the divergence of vertical kinetic energy flux. Nevertheless, the definition of an inertial range (which forms the basis of all cascade theories for the $-5/3$ spectrum) is the same as in two- and three-dimensional turbulence—that is, a range of wavenumbers over which $\langle T(k_h)\rangle \equiv 0$, where $\langle\cdot\rangle$ denotes the ensemble average. In numerical simulations of homogeneous turbulence, the inertial range is often obscured by dissipation, although an inertial range emerges as the Reynolds number of the simulation increases (see Lesieur 1997 for more discussion).

In the present problem, the energy spectrum is additionally influenced by the pressure gradient through $P(\mathbf{k})$. Making the Boussinesq[4] and hydrostatic approximations in (12), we can write

$$\begin{aligned} P(\mathbf{k}) &\approx -\frac{1}{2}\hat{\mathbf{u}}^* \cdot (i\mathbf{k}p') + \text{c.c.} \\ &\approx -\frac{1}{2}(\partial_z\hat{w}^*)p' + \text{c.c.} \\ &\approx -\frac{1}{2}\partial_z(\hat{w}^*\hat{p}') - \frac{1}{2}g\,\hat{w}^*\hat{\rho}' + \text{c.c.} \end{aligned} \tag{13}$$

The first term on the rhs is the convergence of the vertical pressure flux, which corresponds to the flux of IGW energy at lowest order; the second term is the buoyancy flux, which represents the conversion of potential to kinetic energy. Both terms are identically zero in isotropic two- and three-dimensional turbulence when the total wavenumber spectrum is considered. Here, however, they may be nonzero. At statistical stationarity outside the dissipation range, (10) requires that $\langle T(k_h)\rangle = -\langle P(k_h)\rangle$; a nonzero contribution from the pressure term therefore has the potential to undermine inertial range arguments for the mesoscale spectrum. The buoyancy flux presents a similar difficulty for the extension of Kolmogorov's (1941) approach to homogeneous stratified turbulence (e.g., Lumley 1964); here, the problem is further complicated by vertical inhomogeneity.

We have computed $T(\mathbf{k})$ and $P(\mathbf{k})$, calculating the terms inside the $\mathcal{F}$ in (11) and (12) with centered differences and proceeding as with the energy spectrum. Horizontal wavenumber spectra of the energy transfer and pressure term, averaged in z over the upper troposphere and lower stratosphere and in t over $t = 9.5$–10.5 days and 12–13 days, are plotted in Fig. 11. In the upper troposphere for $t = 9.5$–10.5 days, the dominant balance in the mesoscale is between positive $T(k_h)$ and negative $P(k_h)$. Mesoscale energy is deposited by the advective nonlinearity and removed by pressure fluctuations, which are seen in Fig. 12a to be due primarily to the buoyancy flux. For $t = 12$–13 days, the upper troposphere spectra are extremely noisy and cross zero several times in the mesoscale and thus have no dominant sign. In the lower stratosphere, at both times, the overall balance is between positive $P(k_h)$ and negative $T(k_h)$. Mesoscale energy is deposited at this level through the pressure term and removed by the advective

[4] The Boussinesq approximation is reasonable in the 2-km-deep layers over which the spectra are averaged, although it is inappropriate over the full depth of the domain.

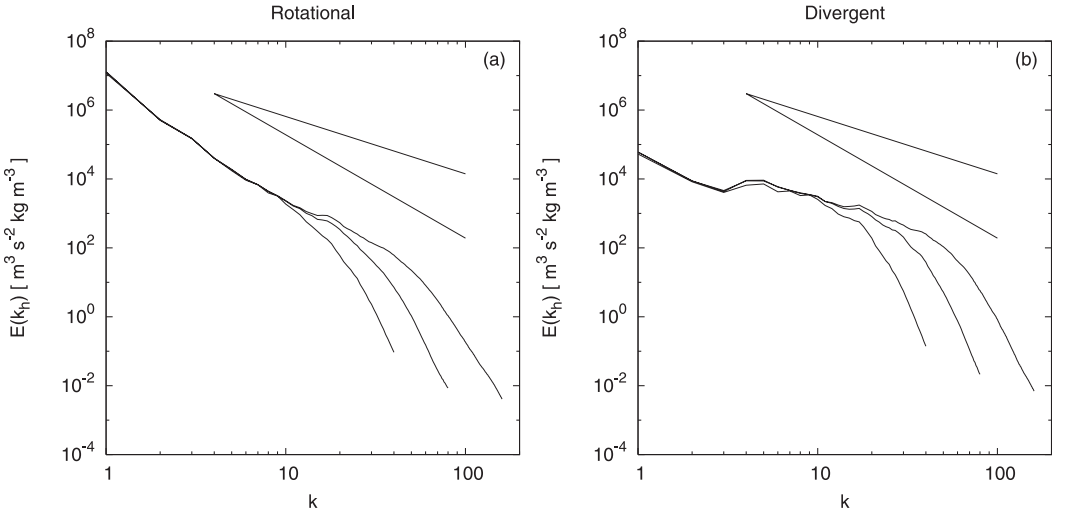

FIG. 9. Horizontal wavenumber spectra of (a) rotational and (b) divergent kinetic energy with $\Delta x = 12.5$, 25, and 50 km. The spectra are averaged in the vertical over the lower stratosphere and in time over $t = 12$–13 days.

nonlinearity. The pressure term here is dominated by vertical pressure flux divergence (Figs. 12b,d) and is consistent with a convergent vertical flux of IGW energy at these levels.

How significant are the deviations of $T(k_h)$ and $P(k_h)$ from zero? The transfer and pressure terms have characteristic inverse time scales at every wavenumber

$$\omega_T(k_h) \equiv \frac{|T(k_h)|}{E(k_h)} \quad \text{and} \quad \omega_P(k_h) \equiv \frac{|P(k_h)|}{E(k_h)}, \tag{14}$$

which can be compared with the eddy frequency (e.g., Lesieur 1997):

$$\omega_e(k_h) \equiv \left[k_h^3 \frac{E(k_h)}{\bar{\rho}(z)}\right]^{1/2}. \tag{15}$$

We compute ω_T, ω_P, and ω_e using the vertically and temporally averaged spectra discussed above; they are plotted in Fig. 13. For ω_e, the averaged energy spectrum is scaled by the average of $\bar{\rho}(z)$ over the layer of interest. In the upper troposphere at early times and the lower stratosphere at both times, ω_T and ω_P have mesoscale values of $O(1)$ day^{-1}; because these values are on the same order as or greater than ω_e, they imply that the transfer and pressure terms are dynamically significantly different from zero. As a result, the dynamics of the

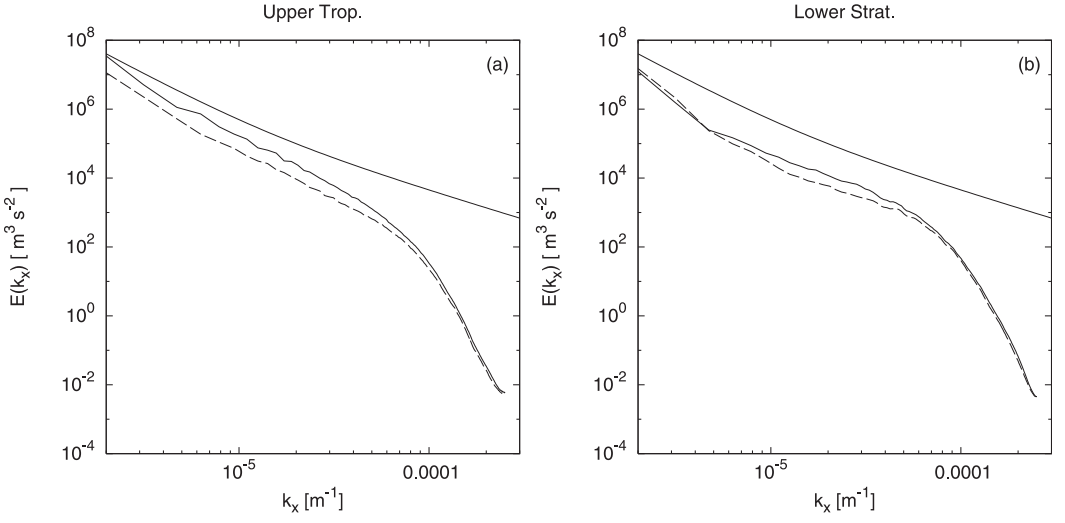

FIG. 10. Zonal wavenumber spectra averaged in the vertical over the (a) upper troposphere and (b) lower stratosphere, in y over $-L_y/4 \le y \le L_y/4$, and in time over $t = 12$–13 days. The smooth solid line is the Lindborg (1999) spectrum; the other curves are total kinetic (solid) and potential (dashed) energy per unit mass.

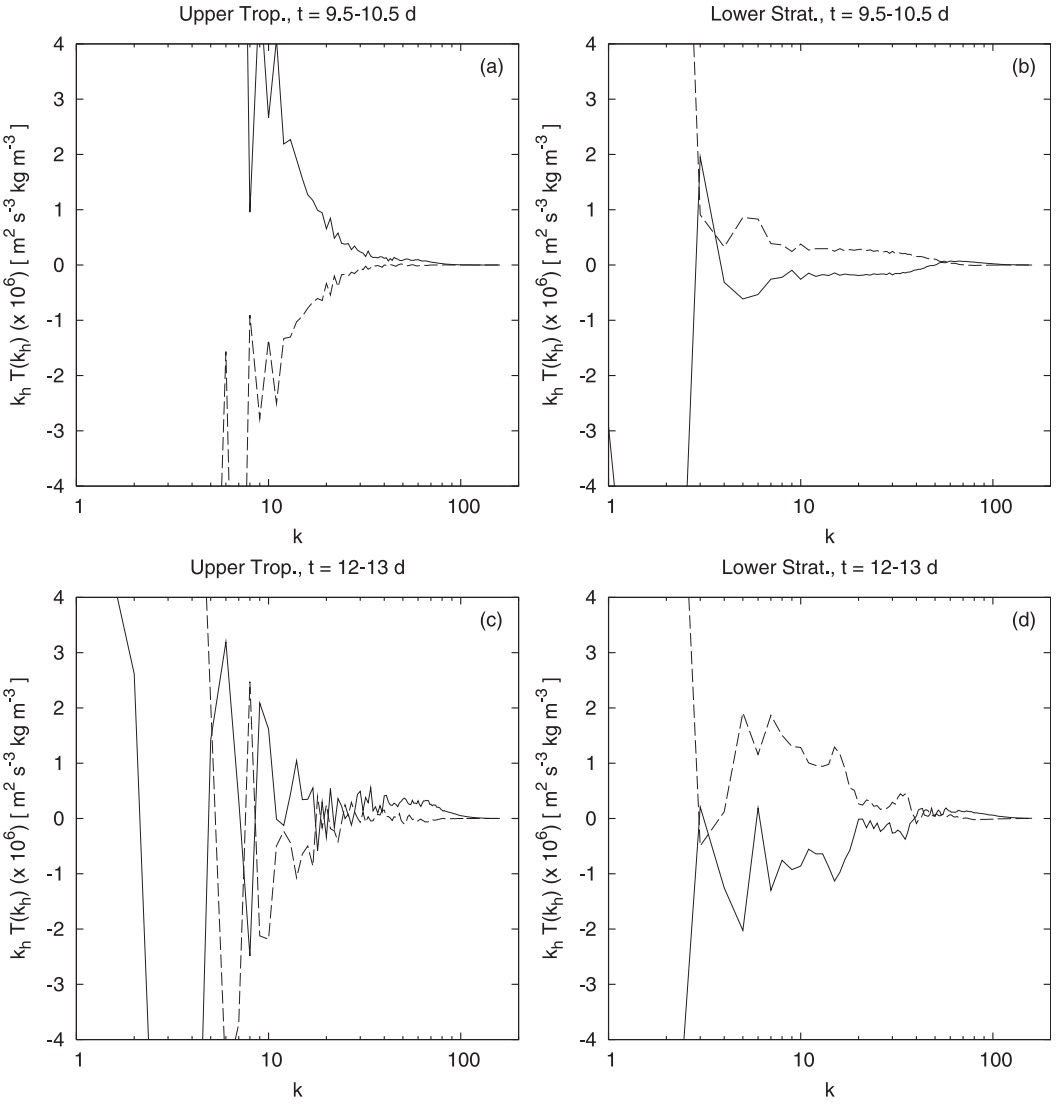

FIG. 11. Horizontal wavenumber spectra of horizontal kinetic energy transfer $T(k_h)$ (solid) and pressure term $P(k_h)$ (dashed), averaged in the vertical over the (left) upper troposphere and (right) lower stratosphere and in time over $t =$ (a),(b) 9.5–10.5 days and (c),(d) 12–13 days. The plotted spectra are multiplied by k_h to preserve area in log-linear coordinates, and the coordinate scale is chosen to emphasize the mesoscale portion of the spectra.

corresponding kinetic energy spectra cannot be described as an inertial range cascade. The nonnegligible contribution of the pressure term to the spectral energy budget is consistent with the findings of Koshyk and Hamilton (2001) for a full general circulation model. In the upper troposphere at later times, by contrast, ω_T and ω_P have values of $O(0.1)$ day^{-1} for wavenumbers smaller than around 40 (wavelengths greater than 100 km), which is significantly smaller than ω_e.

e. Vertical wavenumber spectra

For an additional point of comparison with previous studies, we have computed vertical wavenumber spectra of kinetic energy per unit mass. Tropospheric and stratospheric segments of vertical soundings, from $2 \le z \le 10$ km and $10 \le z \le 16$ km, respectively, were isolated at every horizontal grid point. Linear trends were removed and a Hanning window applied following Nastrom et al. (1997). The resulting spectra, averaged over all x, $-L_y/4 \le y \le L_y/4$, and $12 \le t \le 13$ days, are shown in Fig. 14. Potential temperature spectra (not shown) are sensitive to the presence of fronts and were found to vary significantly with the range of z over which they were computed.

The tropospheric and stratospheric spectra exhibit approximate power-law behavior over almost a decade

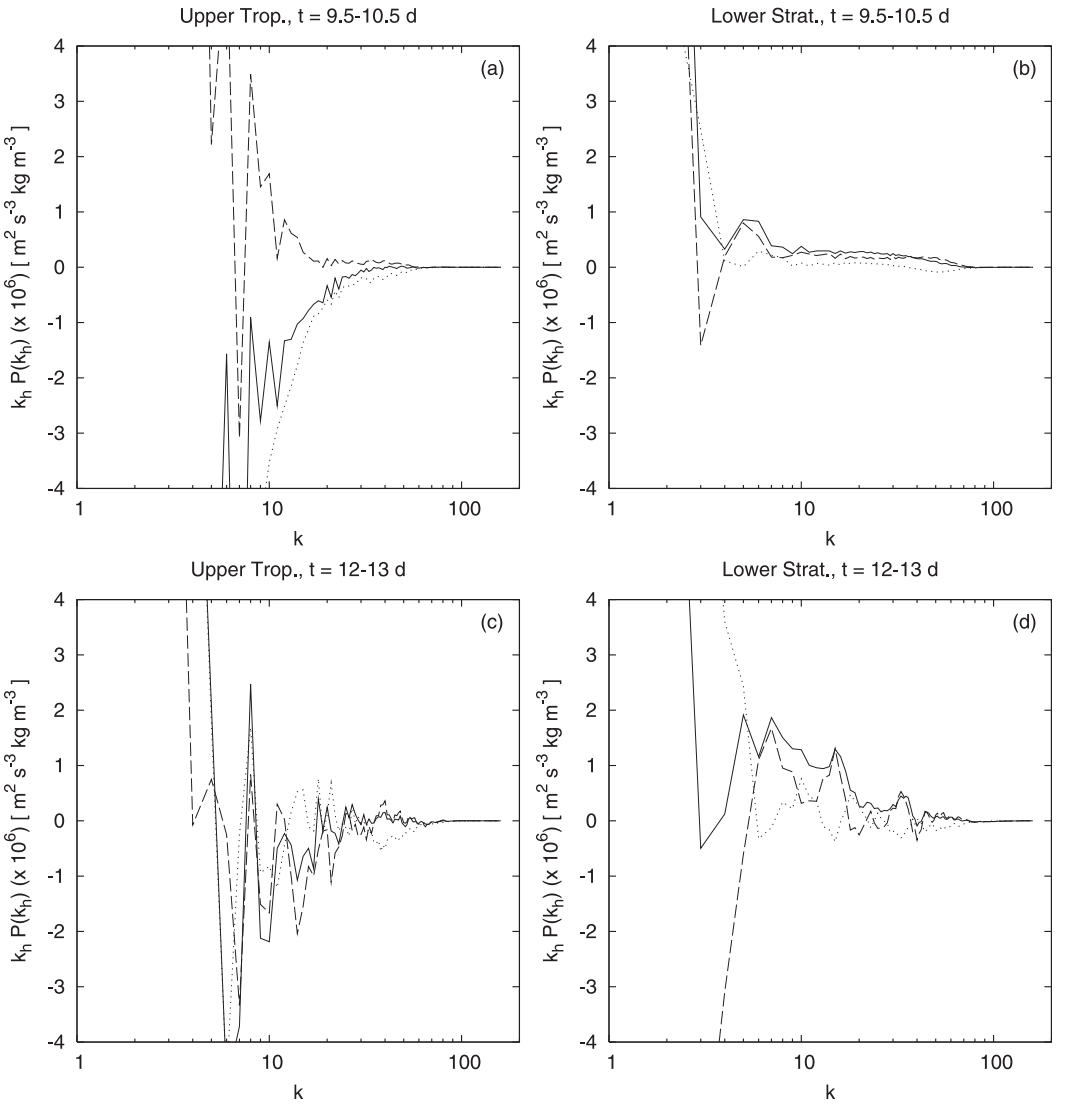

FIG. 12. Horizontal wavenumber spectra of the pressure term $P(k_h)$ (solid), the pressure flux divergence (dashed), and the buoyancy flux (dotted), averaged in the vertical over the (left) upper troposphere and (right) lower stratosphere (right) and in time over $t =$ (a),(b) 9.5–10.5 days and (c),(d) 12–13 days. Other details are as in Fig. 11.

of k_z. The spectral slopes at both levels (measured over $0.003 \leq k_z \leq 0.01$ m^{-1}) are -2.8, which is in remarkable agreement with observations (e.g., Nastrom et al. 1997). The spectra fall off rapidly at larger wavenumbers because of the numerical dissipation implicit in the model's third-order vertical advection scheme. The transition wavenumber is between 0.01 and 0.02 m^{-1}, implying an effective dissipation scale between approximately 300 and 600 m. Structures with vertical scales of 1 km are therefore not strongly damped by numerical diffusion.

The amplitude of the tropospheric spectrum in Fig. 14 is significantly lower than the observed vertical wavenumber spectra. For $k_z = 2\pi/1000$ m^{-1}, we have $k_z E(k_z) \approx 0.06$ m^2 s^{-2}. The corresponding amplitude of the average observed tropospheric spectrum of Nastrom et al. (1997) is an order of magnitude larger. This comparison, however, must be interpreted with caution because fronts, which were omitted by Nastrom et al. (1997), comprise a key component of the dynamics in the present study.

4. Discussion

The development and evolution of the mesoscale kinetic energy spectrum in an idealized dry baroclinic life cycle results from three interacting phenomena: 1) Excitation of IGWs through spontaneous emission, primarily

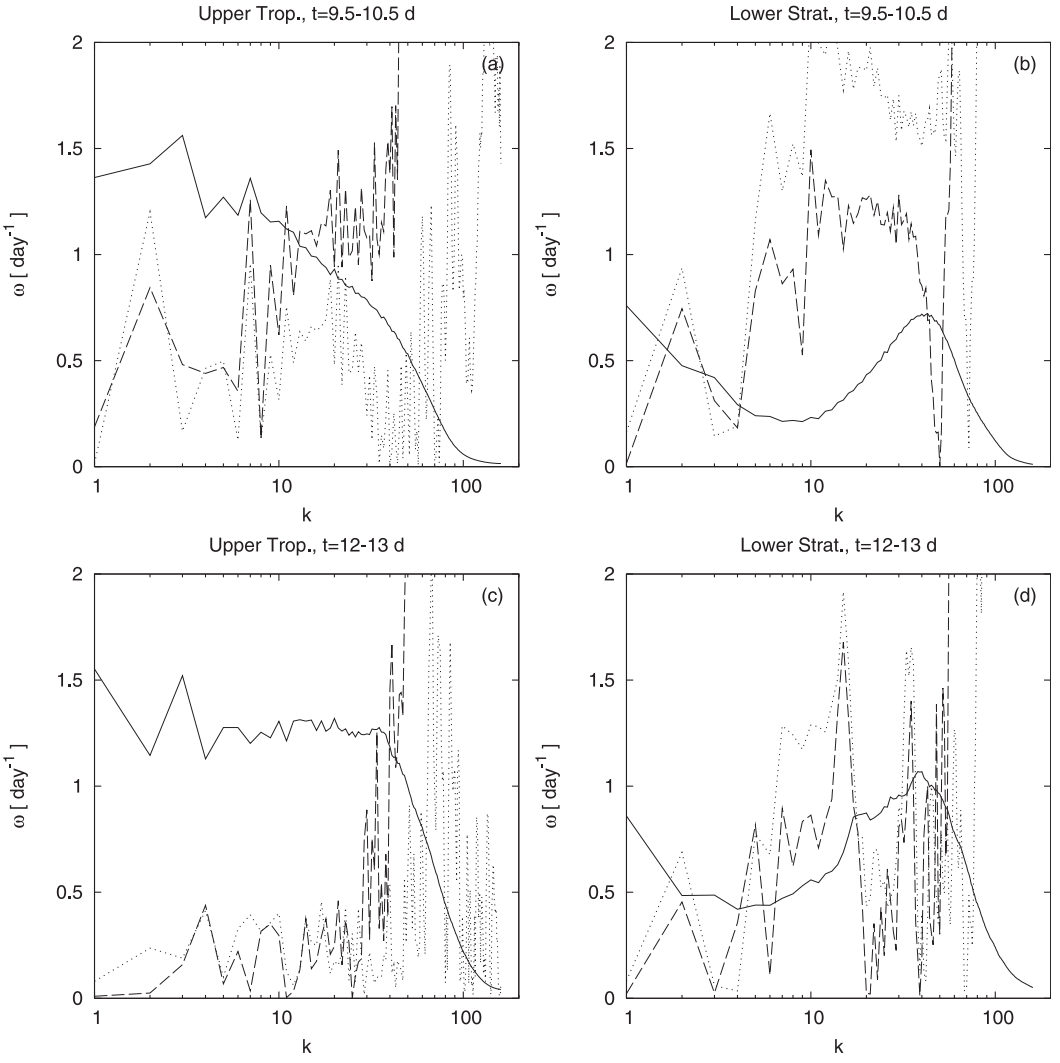

FIG. 13. The eddy frequency $\omega_e(k_h)$ (solid), transfer frequency $\omega_T(k_h)$ (dashed), and pressure frequency $\omega_P(k_h)$ (dotted), computed from spectra averaged in the vertical over the (left) upper troposphere and (right) lower stratosphere and in time over t = (a),(b) 9.5–10.5 days and (c),(d) 12–13 days.

in the upper troposphere, 2) filling out of the kinetic energy spectrum in the upper troposphere through nonlinear interactions, and 3) enhancement of the lower stratospheric spectrum through vertical wave propagation. These are discussed in turn below.

1) Coherent IGW packets emerge early in the nonlinear evolution of the baroclinic wave, presumably via spontaneous emission by the baroclinic vortex; indeed, the other important sources of atmospheric IGWs—topography and moist convection—are explicitly neglected. These waves have $O(100)$-km wavelengths, and although they appear most prominently in the lower stratosphere, previous work on spontaneous emission indicate that their sources lie in the troposphere. Three packets are observed, which are labeled I, II, and III in Fig. 3d:

   (I) A long (≈1000 km) band located east of the trough, forced by frontogenesis near the surface (Snyder et al. 1993);
   (II) A compact (≈500 km) packet located east of the ridge, resembling the waves of Zhang (2004), who suggested that they originate in the midtroposphere above the occlusion; and
   (III) A long band oriented from ridge to trough and spanning the length of the baroclinic wave, as described by Plougonven and Snyder (2005, 2007). These waves are believed to have their source in the jet region of the upper

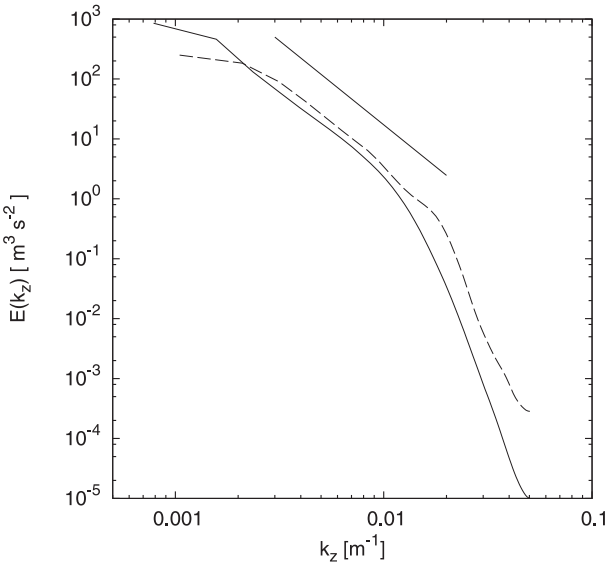

FIG. 14. Vertical wavenumber spectra of kinetic energy per unit mass computed over $2 \leq z \leq 10$ km (solid) and $10 \leq z \leq 16$ km (dashed), averaged over all $x, -L_y/4 \leq y \leq L_y/4$, and $12 \leq t \leq 13$ days. The reference line has a slope of -2.8.

troposphere, and their structure is thought to result from propagation through the deformation and shear of the large-scale flow.

2) The localized packet structure eventually gives way to a more random arrangement of mesoscale disturbances encompassing the entire region of the baroclinic vortex. This transition corresponds to the filling out of the spectrum of horizontally divergent kinetic energy, which takes the form of a $-5/3$ power law in the upper troposphere, where there is negligible net mesoscale energy transfer. Identifying the horizontally divergent velocity field with IGWs, the nonlinear transfer of energy is in general due to wave–wave and wave–vortex interactions. In flows such as the baroclinic life cycle where the large-scale motion is predominantly vortical, theoretical and numerical studies of rotating stratified turbulence suggest that wave–vortex interactions will dominate (Bartello 1995; Waite and Bartello 2006a). Recent work on the propagation of wave packets through a vortical background flow (Bühler and McIntyre 2005; Plougonven and Snyder 2005) supports this conclusion by providing a plausible physical mechanism for the wave–vortex interaction: IGW wavelengths contract as packets are deformed by the straining vortical flow.

   Despite the $-5/3$ spectrum of divergent kinetic energy, no mesoscale shallowing occurs in the total kinetic energy spectrum in the upper troposphere. The rotational kinetic energy, which has a steeper slope of around -3.5—consistent with numerical simulations of QG turbulence (e.g., McWilliams et al. 1994)—dominates the spectrum over the entire range of resolved motion. The rotational and divergent spectra cross near the dissipation range at the mature stage of the baroclinic life cycle. Higher resolution, with $\Delta x \lesssim O(1)$ km and a correspondingly smaller dissipation scale, would therefore likely reveal a transition to a shallower kinetic energy spectrum. However, such a transition would be well inside the mesoscale at wavelengths of approximately 100 km, in contrast to the finding of Nastrom and Gage (1985) that it occurs at the outer limit of the mesoscale.

3) Spontaneously generated IGWs undergo vertical propagation in addition to nonlinear interactions, and this propagation influences the spectral energy budget in the lower stratosphere. The kinetic energy spectrum at these levels exhibits mesoscale shallowing associated with horizontally divergent velocity. Our analysis shows a significant mesoscale forcing of lower stratospheric kinetic energy by vertical pressure flux divergence, consistent with a convergent flux of IGW energy. As a result, the kinetic energy spectrum at this level cannot be explained solely through inertial-range cascade arguments. Indeed, the divergent kinetic energy spectrum in the lower stratospheric mesoscale is nearly identical to that in the upper troposphere at later times, suggesting a strong connection between these levels. Thus, the lower stratospheric $-5/3$ spectrum is a product of the vertical propagation from the upper troposphere coupled with its own nonlinearity.

Despite the idealized nature of our approach, our results display some key similarities with previous observational and numerical studies. First, the large-scale kinetic energy levels in the upper troposphere are in general agreement with the atmospheric data synthesized by Lindborg (1999), confirming that our initial conditions lead to a reasonably energetic synoptic-scale flow with a realistic Rossby number. Second, the ratio of mesoscale kinetic to potential energy is around 2, which is remarkably consistent with observations (Gage and Nastrom 1986). Third, the upper tropospheric kinetic energy spectrum is dominated by rotational motion through the mesoscale, as seen in the analysis of data (Cho et al. 1999; Lindborg 2007) and GCM experiments (Koshyk and Hamilton 2001; Takahashi et al. 2006; Hamilton et al. 2008). Interestingly, this last finding is in contrast to recent NWP simulations that have approximately equal levels of rotational and divergent kinetic energy in the mesoscale (Skamarock and Klemp 2008). Finally, the mesoscale spectrum in the lower

stratosphere is shallow and dominated by divergent kinetic energy, as in the stratospheric spectra of Koshyk and Hamilton (2001). However, the rotational kinetic energy spectra in the lower stratosphere of our simulations do not shallow to nearly the same degree seen in Koshyk and Hamilton (2001).

At the same time, there are major differences between our results and these previous investigations. Most significantly, the steep kinetic energy spectrum in the lower troposphere does not display the mesoscale shallowing seen in data (Nastrom and Gage 1985) and full-physics numerical experiments (e.g., Koshyk and Hamilton 2001; Skamarock 2004; Takahashi et al. 2006; Hamilton et al. 2008; Skamarock and Klemp 2008). This underenergized mesoscale is reminiscent of the dry dynamical core GCM experiments of Takahashi et al. (2006) and Hamilton et al. (2008) in which, as in our study, moist physics and topography were omitted. They found that the absence of these effects resulted in a steeper, lower-amplitude mesoscale kinetic energy spectrum. In contrast to our findings, however, the dry dynamical core GCM did yield a transition to a shallow spectrum well inside the mesoscale. This distinction may result from the forced-dissipative nature of the GCM simulations, which likely leads to a stronger downscale energy flux than the coherent baroclinic wave considered here. Nevertheless, our results provide further evidence for the conclusion of Hamilton et al. (2008) that physical processes other than a downscale cascade are responsible for maintaining observed mesoscale kinetic energy levels.

It is also possible that the mesoscale flow in our simulations and others based on GCMs and NWP models is significantly influenced by the numerical resolution. Simulations in the literature from GCMs and NWP models clearly have insufficient vertical resolution to capture stratified turbulence, which was proposed by Lindborg (2006) to drive the $-5/3$ mesoscale energy spectrum. A necessary condition for stratified turbulence is that vertical scales of U/N (around 1 km in the troposphere) be resolved and not damped by explicit or numerical vertical diffusion (Waite and Bartello 2004; Lindborg 2006; Brethouwer et al. 2007). As discussed in section 3e, this condition is satisfied in our simulation. Nevertheless, a mesoscale stratified turbulence cascade does not occur. We cannot rule out the possibility that additional vertical and horizontal resolution would allow a transition to some form of stratified turbulence and a horizontal wavenumber spectrum in better agreement with observations.

On the other hand, if moist convection and flow over topography are essential for the maintenance of a realistic mesoscale spectrum, a fundamental question is whether their effects are predominantly large scale or whether they force the mesoscale directly. Such direct forcing would violate the inertial range hypothesis that underlies all cascade theories for the mesoscale $-5/3$ spectrum. Our results in the lower stratosphere show that this hypothesis can be violated—here, by vertical pressure flux divergence—without changing the end result. An inertial range cascade is a sufficient but not necessary condition for the emergence of a $-5/3$ spectrum. The complex interplay between direct forcing and nonlinear interactions in the mesoscale clearly deserves further study.

Acknowledgments. The authors wish to thank Richard Rotunno and two anonymous referees for helpful comments on the manuscript, and George Bryan, Riwal Plougonven, and William Skamarock for assistance with the setup of the numerical simulations. MLW gratefully acknowledges the support of the NCAR Advanced Study Program. CS acknowledges support from the National Science Foundation through Grant CMG-0327582.

REFERENCES

Bartello, P., 1995: Geostrophic adjustment and inverse cascades in rotating stratified turbulence. *J. Atmos. Sci.,* **52,** 4410–4428.

Boer, G. J., and T. G. Shepherd, 1983: Large-scale two-dimensional turbulence in the atmosphere. *J. Atmos. Sci.,* **40,** 164–184.

Brethouwer, G., P. Billant, E. Lindborg, and J.-M. Chomaz, 2007: Scaling analysis and simulation of strongly stratified turbulent flows. *J. Fluid Mech.,* **585,** 343–368.

Bühler, O., and M. E. McIntyre, 2005: Wave capture and wave–vortex duality. *J. Fluid Mech.,* **534,** 67–95.

Bush, A. B. G., and W. R. Peltier, 1994: Tropopause folds and synoptic-scale baroclinic wave life cycles. *J. Atmos. Sci.,* **51,** 1581–1604.

Charney, J. G., 1971: Geostrophic turbulence. *J. Atmos. Sci.,* **28,** 1087–1095.

Cho, J. Y. N., R. E. Newell, and J. D. Barrick, 1999: Horizontal wavenumber spectra of winds, temperature, and trace gases during the Pacific Exploratory Missions: 2. Gravity waves, quasi-two-dimensional turbulence, and vortical modes. *J. Geophys. Res.,* **104,** 16 297–16 308.

Dewan, E. M., 1979: Stratospheric wave spectra resembling turbulence. *Science,* **204,** 832–835.

——, 1997: Saturated-cascade similitude theory of gravity wave spectra. *J. Geophys. Res.,* **102,** 29 799–29 817.

Fritts, D. C., and G. D. Nastrom, 1992: Sources of mesoscale variability of gravity waves. Part II: Frontal, convective, and jet stream excitation. *J. Atmos. Sci.,* **49,** 111–127.

Gage, K. S., 1979: Evidence for a $k^{-5/3}$ law inertial range in mesoscale two-dimensional turbulence. *J. Atmos. Sci.,* **36,** 1950–1954.

——, and G. D. Nastrom, 1986: Theoretical interpretation of atmospheric wavenumber spectra of wind and temperature observed by commercial aircraft during GASP. *J. Atmos. Sci.,* **43,** 729–740.

Hamilton, K., Y. O. Takahashi, and W. Ohfuchi, 2008: Mesoscale spectrum of atmospheric motions investigated in a very fine

resolution global general circulation model. *J. Geophys. Res.,* **113,** D18110, doi:10.1029/2008JD009785.

Herring, J. R., and O. Métais, 1989: Numerical experiments in forced stably stratified turbulence. *J. Fluid Mech.,* **202,** 97–115.

Kitamura, Y., and Y. Matsuda, 2006: The k_h^{-3} and $k_h^{-5/3}$ energy spectra in stratified turbulence. *Geophys. Res. Lett.,* **33,** L05809, doi:10.1029/2005GL024996.

Kolmogorov, A. N., 1941: The local structure of turbulence in incompressible viscous fluid for very large Reynolds number. *Dokl. Akad. Nauk SSSR,* **30,** 301–305.

Koshyk, J. N., and K. Hamilton, 2001: The horizontal kinetic energy spectrum and spectral budget simulated by a high-resolution troposphere–stratosphere–mesosphere GCM. *J. Atmos. Sci.,* **58,** 329–348.

Kraichnan, R. H., 1967: Inertial ranges in two-dimensional turbulence. *Phys. Fluids,* **10,** 1417–1423.

Lelong, M.-P., and J. J. Riley, 1991: Internal wave–vortical mode interactions in strongly stratified flows. *J. Fluid Mech.,* **232,** 1–19.

Lesieur, M., 1997: *Turbulence in Fluids*. 3rd ed. Kluwer, 515 pp.

Lilly, D. K., 1983: Stratified turbulence and the mesoscale variability of the atmosphere. *J. Atmos. Sci.,* **40,** 749–761.

——, G. Bassett, K. Droegemeier, and P. Bartello, 1998: Stratified turbulence in the atmospheric mesoscale. *Theor. Comput. Fluid Dyn.,* **11,** 139–153.

Lindborg, E., 1999: Can the atmospheric kinetic energy spectrum be explained by two-dimensional turbulence? *J. Fluid Mech.,* **388,** 259–288.

——, 2006: The energy cascade in a strongly stratified fluid. *J. Fluid Mech.,* **550,** 207–242.

——, 2007: Horizontal wavenumber spectra of vertical vorticity and horizontal divergence in the upper troposphere and lower stratosphere. *J. Atmos. Sci.,* **64,** 1017–1025.

——, and J. Y. N. Cho, 2001: Horizontal velocity structure functions in the upper troposphere and lower stratosphere. 2. Theoretical considerations. *J. Geophys. Res.,* **106,** 10 233–10 241.

Lumley, J. L., 1964: The spectrum of nearly inertial turbulence in a stably stratified fluid. *J. Atmos. Sci.,* **21,** 99–102.

McWilliams, J. C., J. B. Weiss, and I. Yavneh, 1994: Anisotropy and coherent vortex structures in planetary turbulence. *Science,* **264,** 410–413.

Methven, J., and B. Hoskins, 1998: Spirals in potential vorticity. Part I: Measures of structure. *J. Atmos. Sci.,* **55,** 2053–2066.

Nastrom, G. D., and K. S. Gage, 1985: A climatology of atmospheric wavenumber spectra observed by commercial aircraft. *J. Atmos. Sci.,* **42,** 950–960.

——, T. E. Van Zandt, and J. M. Warnock, 1997: Vertical wavenumber spectra of wind and temperature from high-resolution balloon soundings over Illinois. *J. Geophys. Res.,* **102,** 6685–6701.

O'Sullivan, D., and T. J. Dunkerton, 1995: Generation of inertia–gravity waves in a simulated life cycle of baroclinic instability. *J. Atmos. Sci.,* **52,** 3695–3716.

Plougonven, R., and C. Snyder, 2005: Gravity waves excited by jets: Propagation versus generation. *Geophys. Res. Lett.,* **32,** L18802, doi:10.1029/2005GL023730.

——, and ——, 2007: Inertia–gravity waves spontaneously generated by jets and fronts. Part I: Different baroclinic life cycles. *J. Atmos. Sci.,* **64,** 2502–2520.

Polavarapu, S. M., and W. R. Peltier, 1990: The structure and nonlinear evolution of synoptic-scale cyclones: Life cycle simulations with a cloud-scale model. *J. Atmos. Sci.,* **47,** 2645–2673.

Ramamurthy, M. K., R. M. Rauber, B. P. Collins, and N. K. Malhotra, 1993: A comparative study of large-amplitude gravity-wave events. *Mon. Wea. Rev.,* **121,** 2951–2974.

Riley, J. J., and M.-P. Lelong, 2000: Fluid motions in the presence of strong stable stratification. *Annu. Rev. Fluid Mech.,* **32,** 613–657.

——, and S. M. de Bruyn Kops, 2003: Dynamics of turbulence strongly influenced by buoyancy. *Phys. Fluids,* **15,** 2047–2059.

Rotunno, R., W. C. Skamarock, and C. Snyder, 1994: An analysis of frontogenesis in numerical simulations of baroclinic waves. *J. Atmos. Sci.,* **51,** 3373–3398.

Shutts, G., 2005: A kinetic energy backscatter algorithm for use in ensemble prediction systems. *Quart. J. Roy. Meteor. Soc.,* **131,** 3079–3102.

Skamarock, W. C., 2004: Evaluating mesoscale NWP models using kinetic energy spectra. *Mon. Wea. Rev.,* **132,** 3019–3032.

——, and J. B. Klemp, 2008: A time-split nonhydrostatic atmospheric model for weather research and forecasting applications. *J. Comput. Phys.,* **227,** 3465–3485.

——, ——, J. Dudhia, D. O. Gill, D. M. Barker, W. Wang, and J. G. Powers, 2005: A description of the Advanced Research WRF Version 2. NCAR Tech. Note NCAR/TN-468+STR, 88 pp.

Snyder, C., W. C. Skamarock, and R. Rotunno, 1991: A comparison of primitive-equation and semigeostrophic simulations of baroclinic waves. *J. Atmos. Sci.,* **48,** 2179–2194.

——, ——, and ——, 1993: Frontal dynamics near and following frontal collapse. *J. Atmos. Sci.,* **50,** 3194–3211.

——, D. J. Muraki, R. Plougonven, and F. Zhang, 2007: Inertia–gravity waves generated within a dipole vortex. *J. Atmos. Sci.,* **64,** 4417–4431.

Takahashi, Y. O., K. Hamilton, and W. Ohfuchi, 2006: Explicit global simulation of the mesoscale spectrum of atmospheric motions. *Geophys. Res. Lett.,* **33,** L12812, doi:10.1029/2006GL026429.

Thorncroft, C. D., B. J. Hoskins, and M. E. McIntyre, 1993: Two paradigms of baroclinic-wave life-cycle behaviour. *Quart. J. Roy. Meteor. Soc.,* **119,** 17–55.

Tulloch, R., and K. S. Smith, 2006: A theory for the atmospheric energy spectrum: Depth-limited temperature anomalies at the tropopause. *Proc. Natl. Acad. Sci. USA,* **103,** 14 690–14 694.

Tung, K. K., and W. W. Orlando, 2003: The k^{-3} and $k^{-5/3}$ energy spectrum of atmospheric turbulence: Quasigeostrophic two-level model simulation. *J. Atmos. Sci.,* **60,** 824–835.

Uccellini, L. W., and S. E. Koch, 1987: The synoptic setting and possible source mechanisms for mesoscale gravity wave events. *Mon. Wea. Rev.,* **115,** 721–729.

VanZandt, T. E., 1982: A universal spectrum of buoyancy waves in the atmosphere. *Geophys. Res. Lett.,* **9,** 575–578.

Viudez, A., 2007: The origin of the stationary frontal wave packet spontaneously generated in rotating stratified vortex dipoles. *J. Fluid Mech.,* **593,** 359–383.

Waite, M. L., and P. Bartello, 2004: Stratified turbulence dominated by vortical motion. *J. Fluid Mech.,* **517,** 281–308.

——, and ——, 2006a: Stratified turbulence generated by internal gravity waves. *J. Fluid Mech.,* **546,** 313–339.

——, and ——, 2006b: The transition from geostrophic to stratified turbulence. *J. Fluid Mech.,* **568,** 89–108.

Wicker, L. J., and W. C. Skamarock, 2002: Time-splitting methods for elastic models using forward time schemes. *Mon. Wea. Rev.,* **130,** 2088–2097.

Zhang, F., 2004: Generation of mesoscale gravity waves in upper-tropospheric jet–front systems. *J. Atmos. Sci.,* **61,** 440–457.